SUPERCONDUCTORS

2015 © The Authors, some rights reserved; exclusive licensee American Association for the Advancement of Science. Distributed under a Creative Commons Attribution NonCommercial License 4.0 (CC BY-NC).
10.1126/sciadv.1500033

Imaging atomic-scale effects of high-energy ion irradiation on superconductivity and vortex pinning in Fe(Se,Te)

Freek Massee,[1,2,3]*† Peter Oliver Sprau,[1,2†] Yong-Lei Wang,[4] J. C. Séamus Davis,[1,2,5,6] Gianluca Ghigo,[7,8] Genda Gu,[1] Wai-Kwong Kwok[4]

Maximizing the sustainable supercurrent density, J_C, is crucial to high-current applications of superconductivity. To achieve this, preventing dissipative motion of quantized vortices is key. Irradiation of superconductors with high-energy heavy ions can be used to create nanoscale defects that act as deep pinning potentials for vortices. This approach holds unique promise for high-current applications of iron-based superconductors because J_C amplification persists to much higher radiation doses than in cuprate superconductors without significantly altering the superconducting critical temperature. However, for these compounds, virtually nothing is known about the atomic-scale interplay of the crystal damage from the high-energy ions, the superconducting order parameter, and the vortex pinning processes. We visualize the atomic-scale effects of irradiating $FeSe_xTe_{1-x}$ with 249-MeV Au ions and find two distinct effects: compact nanometer-sized regions of crystal disruption or "columnar defects," plus a higher density of single atomic site "point" defects probably from secondary scattering. We directly show that the superconducting order is virtually annihilated within the former and suppressed by the latter. Simultaneous atomically resolved images of the columnar crystal defects, the superconductivity, and the vortex configurations then reveal how a mixed pinning landscape is created, with the strongest vortex pinning occurring at metallic core columnar defects and secondary pinning at clusters of point-like defects, followed by collective pinning at higher fields.

Iron-based superconductors (*1*) are promising for high J_C applications (*2*) because of a nexus of several materials characteristics (*3*). First, the maximum critical field H_{C2} is very high at low temperatures (*4*, *5*), the compounds also exhibit rather isotropic superconductivity. Second, as in the cuprates (*6*), J_C can be strongly enhanced by high-energy ion irradiation (*2*, *7*). Finally, the irradiation leaves T_C virtually unchanged to a degree unknown in cuprate high-temperature superconductors. Therefore, if engineered control of J_C could be achieved under these circumstances, these materials could be very favorable for high-current/high-field applications. The theoretical understanding necessary for such materials engineering requires specific atomic-scale knowledge, including the structure of ion-induced columnar defects, along with their local influence on the superconductivity. For example, detailed knowledge of a columnar defect's internal conductivity and of its size with respect to the superconducting coherence length is required to quantitatively predict its interaction with a vortex core (*8*, *9*). Imaging of high-energy ion-induced columnar defects has been achieved using transmission electron microscopy (*6*, *10*–*14*), and visualization of irradiation-induced disordered vortex configurations (*15*, *16*) has been achieved by scanning tunneling microscopy (STM). However, to our knowledge, simultaneous atomic-scale visualization of the effects of high-energy ions on the crystal, the resulting impact on the superconductivity, and the consequent responses of the pinned vortex configurations have not been achieved for any type of superconductor.

To initiate such studies, we chose $FeSe_xTe_{1-x}$ (*17*). In bulk single crystal form, its transition temperature can reach up to ~15 K with H_{C2} at tens of tesla (*18*); in thin films, critical fields are enhanced and T_C ~100 K has been reported for unit-cell-thick monolayers of FeSe (*19*). Here, we use a ^{3}He-refrigerator–based spectroscopic imaging scanning tunneling microscope (SI-STM) (*20*) into which the $FeSe_xTe_{1-x}$ samples are inserted and cleaved in a cryogenic ultrahigh vacuum at T <20 K. This technique consists of making atomically resolved and registered images of the surface topography $T(\mathbf{r})$ simultaneously with tip-sample differential tunneling conductance images $g(\mathbf{r},E = eV) \equiv dI/dV(\mathbf{r},E = eV)$ measured as a function of both location $\mathbf{r}$ and electron energy E. Figure 1A shows a typical $T(\mathbf{r})$ of the TeSe termination layer with individual Te/Se atomic sites clearly visible (*21*, *22*). In the superconducting phase at $T = 0.25$ K, our measured $g(\mathbf{r},E)$ spectra are then fully gapped with clear superconducting coherence peaks (*23*) (arrows, Fig. 1B) and a spatially homogeneous superconducting energy gap Δ (Fig. 1B). Upon application of the magnetic field, the Abrikosov vortex lattice is observed in the zero-bias conductance images, as shown in Fig. 1C. The autocorrelation function, depicted in Fig. 1D, exhibits a hexagonal pattern, pointing to a real space vortex lattice that remains overall hexagonally ordered.

Single crystals of $FeSe_{0.45}Te_{0.55}$ from the same batch as in Fig. 1 were then irradiated with 249-MeV Au ions using a fluence of 1.93×10^{15} m^{-2} so that the "dose equivalent field" is B_ϕ = 4 T (this is the field ideally corresponding to a fluxon per incident ion). However, few-hundreds-MeV heavy ions in metallic Fe-based superconductors create defect tracks that are expected to be discontinuous; thus, the actual columnar defect density in a given crystal layer may be lower than the fluence (*12*). Figure 2A shows a high-resolution $T(\mathbf{r})$ typical of the irradiated $FeSe_xTe_{1-x}$ crystals, in which two striking new features are apparent. The first consists of large (radius ~1.5 nm) amorphous regions (for example, red circles in Fig. 2A) with a surface coverage equivalent to a matching magnetic field of about 2 T in this field of view (FOV). The second type of feature occurs in larger numbers and consists of an atomic-scale point defect

[1]Condensed Matter Physics & Materials Science Department, Brookhaven National Laboratory, Upton, NY 11973, USA. [2]Laboratory of Atomic and Solid State Physics, Department of Physics, Cornell University, Ithaca, NY 14853, USA. [3]Laboratoire de Physique des Solides, Universite Paris-Sud, 91405 Orsay, France. [4]Materials Science Division, Argonne National Laboratory, Argonne, IL 60439, USA. [5]School of Physics and Astronomy, University of St Andrews, St Andrews, Fife KY16 9SS, UK. [6]Kavli Institute at Cornell for Nanoscale Science, Cornell University, Ithaca, NY 14853, USA. [7]Department of Applied Science and Technology, Politecnico di Torino, 10129 Torino, Italy. [8]Istituto Nazionale di Fisica Nucleare, Sezione di Torino, 10125 Torino, Italy.
*Corresponding author. E-mail: freek.massee@u-psud.fr
†These authors contributed equally to this work.

Downloaded from https://www.science.org at Nanjing University on August 23, 2026

(for example, blue circles) centered in between Se/Te sites, thus, at the Fe site in the layer below the surface. These are reminiscent of excess iron atoms observed in other studies (*21*, *24*). Because we never see such excess Fe atoms on multiple pristine samples from the same growth batch, we speculate that the heavy ion irradiation has displaced Fe atoms into these sites. The matrix in which these two ion-induced defect types are detected in exhibits an unperturbed $FeSe_{0.45}Te_{0.55}$ termination layer morphology (inset, Fig. 2A). See section II of the Supplementary Materials for additional, more detailed studies of these two types of ion-induced crystal defect.

Atomic-scale imaging reveals that columnar defects exhibit an amorphous crystal structure in a region with a diameter of about 3 nm. For each, the impact on superconductivity is its annihilation, as shown in Fig. 2B, which compares the average $g(E)$ spectrum (gray) to that at the center of ion-induced columnar defects (red). These data directly demonstrate that the columnar defect cores of Fe(Se,Te) are metallic. By contrast, the signature of superconductivity in each point defect spectrum (blue, Fig. 2C) is significantly suppressed relative to the average $g(E)$ spectrum (gray, Fig. 2C), meaning that these regions should individually provide weaker pinning sites. A discussion of the properties of the defects far beyond the energy scale of superconductivity is available in the Supplementary Materials. From a global perspective, the effects on the superconductivity of the high-energy ion irradiation are both profound and somewhat unexpected. Specifically, the $g(\mathbf{r},E)$ images measured on irradiated samples are no longer characterized by a homogeneous, full superconducting gap, but show a strong spatial variation with a finite differential conductance at zero bias everywhere. To illustrate the effects on the superconductivity in the FOV of Fig. 2A, we define the normalized function

$$F(\mathbf{r}) = \frac{g(\mathbf{r},\Delta) - g(\mathbf{r},0)}{\overline{g(\mathbf{r})}} \quad (1)$$

as a measure of the strength of the spectral signature of superconductivity. Here, $g(\mathbf{r},\Delta)$ is the sum of $g(\mathbf{r},E)$ over the energy region of coherence peaks $\Delta \sim (\pm 1.5 \leq E \leq \pm 2.5$ meV), $g(\mathbf{r},0)$ is the sum of $g(\mathbf{r},E)$ over the energy window centered on zero ($-0.5 \leq E \leq 0.5$ meV), whereas the average in the denominator runs over $E = \pm 5$ meV. Then, for $F > 1$, the superconducting peak-to-dip difference is at least as large as the approximate normal-state absolute conductance; hence, there is a well-defined superconducting spectral signature. For $F < 0.2$, the superconducting signature is on the order of, or smaller than, the noise level, meaning that superconductivity is completely suppressed. The $F(\mathbf{r})$ image measured in the FOV of Fig. 2A is shown in Fig. 2D and reveals the atomic-scale spatial arrangements of damage to the superconductivity as a result of heavy ion irradiation in Fe(Se,Te) (see section III of the Supplementary Materials for comparison with the identical analysis of the pristine sample). Less than 50% of this (and all equivalent) FOV is weakly affected by irradiation (dark blue). The three columnar defects each exhibit complete suppression of the superconductivity but only within a radius of about 1.5 nm so that, in themselves, they could not affect the overall superconductivity to the degree observed. It is the combined effect of the more than 20-point defects that dominate, especially when several are clustered within a mutual radius of ~3 nm with a resulting strong suppression of superconductivity. Additional analysis on the relationship between point defect position and order parameter suppression is provided in the Supplementary Materials. The further

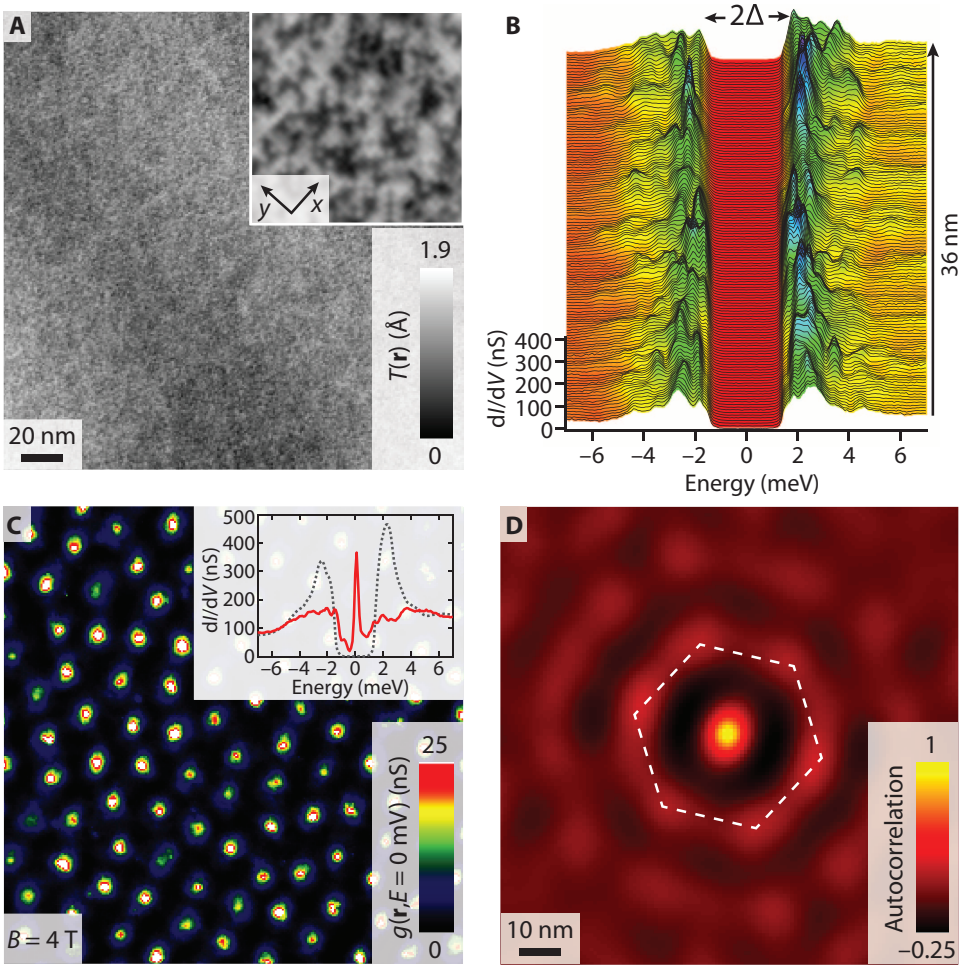

Fig. 1. Visualizing superconductivity in pristine Fe(Se,Te). (**A**) Large, atomically resolved constant current topograph $T(\mathbf{r})$ of $FeSe_{0.45}Te_{0.55}$. The inset shows an enlargement of the atomic lattice using the same color scale. (**B**) Differential conduction spectra at 270 mK taken along a line just outside the FOV shown in (A): all spectra are fully gapped with clear coherence peaks (indicated by arrows). The multitude of peaks outside the gap reflects the multiband nature of the system. (**C**) Vortex lattice of pristine Fe(Se,Te). The lattice is predominantly hexagonal with only minor distortions because of native pinning of vortices. The inset shows the FOV average spectrum away from vortices (dashed) and a typical spectrum taken at the core of a vortex (red) at 270 mK. (**D**) Autocorrelation of (C) exemplifying the predominance of the hexagonal vortex structure.

Downloaded from https://www.science.org at Nanjing University on August 23, 2026

remarkable thing about this situation is that T_C is barely suppressed (by less than 1 K) and J_C is strongly enhanced (see section I of the Supplementary Materials). The objective is to understand the microscopics of vortex pinning by this complex superconducting landscape.

The field dependence of the vortex distribution process in irradiated Fe(Se,Te) is next determined. In an identical FOV, we measure a series of $T = 0.25$ K electronic structure images $g(\mathbf{r}, E, B)$, where B is the magnitude of the magnetic field applied perpendicular to the crystal surface. The classic signature of a vortex core when observed by measuring $g(\mathbf{r},E)$ is the suppression of coherence peaks surrounding $E \sim \pm\Delta$ and the increase in zero-bias conductance surrounding $E \sim 0$. A reasonable and practical way to detect vortices is to image the function

$$S(\mathbf{r}) = \big(g(\mathbf{r},0,B) - g(\mathbf{r},0,0)\big) - \big(g(\mathbf{r},\Delta_-,B) - g(\mathbf{r},\Delta_-,0) + g(\mathbf{r},\Delta_+,B) - g(\mathbf{r},\Delta_+,0)\big)/2 \quad (2)$$

which combines spectral weight from both primary phenomena near the core. Surprisingly, however, as exemplified in Fig. 3, the signature of vortices in the presence of columnar defects is not of this simple form. For fields up to about 2 T for this FOV, we hardly see this classic signature of the vortex cores being introduced at all. Instead, the most common observation is that a circular "halo" is detected in $S(\mathbf{r})$ surrounding columnar defects identified from the local crystal damage in $T(\mathbf{r})$. Figure 3A shows a small FOV with about seven columnar defects, whereas Fig. 3B shows high-resolution $S(\mathbf{r})$ measured at $B = 2$ T. A vortex is (collectively) pinned within the red box in both figures, which does not contain a columnar defect, and its signature in $S(\mathbf{r})$ is as expected. However, the vortex pinned at a columnar defect shown with the yellow box in both images has a very distinct signature consisting of a halo in $S(\mathbf{r})$ surrounding the columnar defect; this vortex halo signature is found at many columnar defects whose average topographic signature is shown in Fig. 3D and whose average $S(\mathbf{r})$ is shown in Fig. 3C. A comparison between halo signature and observable vortices is presented in the Supplementary Materials. The concept is that the halo is the signature of a pinned fluxon, but one where the conventional vortex core spectrum cannot be detected as the fluxon resides on a location of suppressed superconductivity at zero magnetic field.

Once the applied field exceeds about 2 T for this FOV, the additional vortex core locations become more easily observable, exhibiting a reasonable example of the classic signature. In terms of $S(\boldsymbol{r})$, this is expected to be a bright circularly symmetric region of high |S| and of radius near one coherence length, which is what is observed. Under

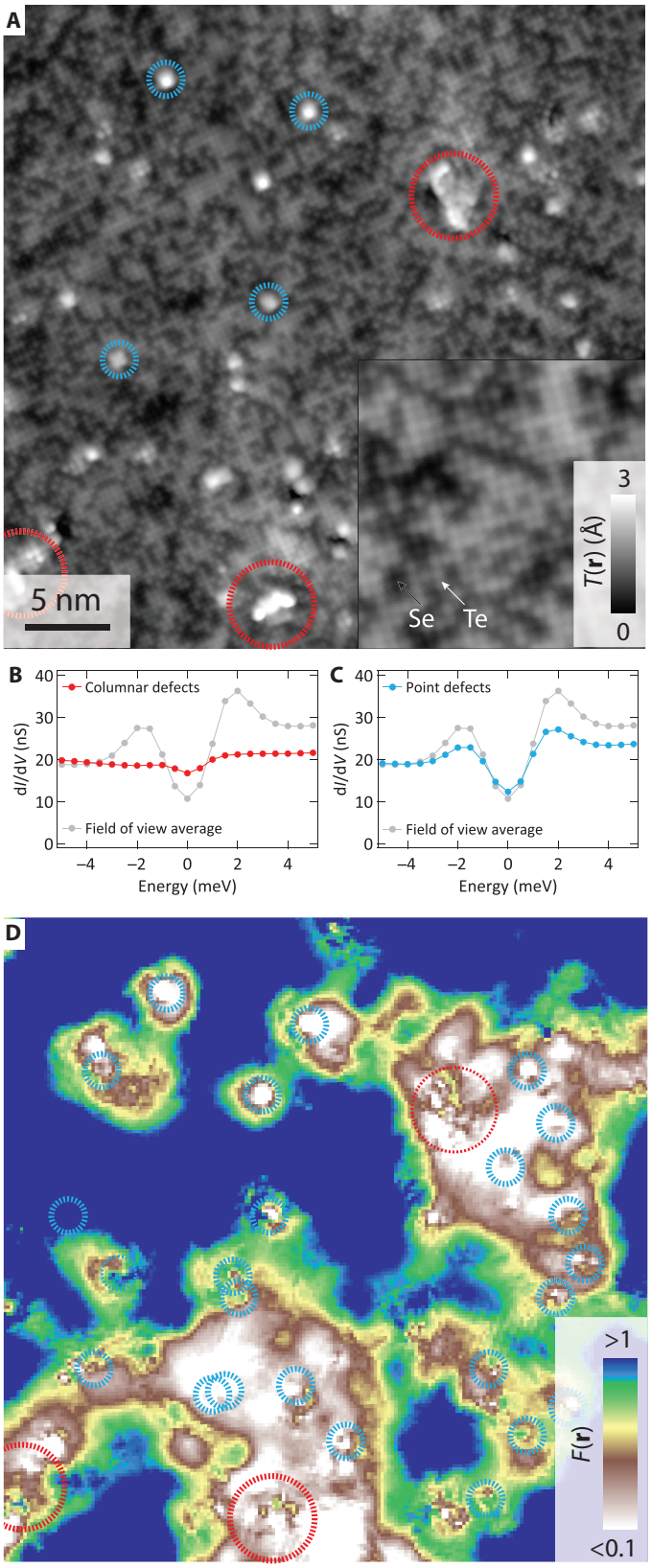

Fig. 2. Impact on Fe(Se,Te) superconductivity of heavy ion irradiation. (**A**) High-resolution $T(\mathbf{r})$ of heavy ion–irradiated $FeSe_{0.45}Te_{0.55}$. As for the pristine sample, the predominant feature is the binary Se/Te surface appearance (inset). Red and blue circles indicate the columnar and point defects that are both only observed after irradiation. Depending on the FOV, the observed damage track density during our SI-STM studies varies between 2-and 4-T effective dose. This may be because the columnar defect tracks are discontinuous or because the distribution is sufficiently heterogeneous that the FOV may not be large enough for an accurate statistical count. (**B**) Average differential conduction spectrum at 1.2 K of columnar defects in (A): the superconducting signature in the tunnel spectrum is completely suppressed. (**C**) Average differential conduction spectrum at 1.2 K of point defects in (A): the superconducting signature in the tunnel spectrum shows significant reduction. (**D**) $F(\mathbf{r})$ as defined in the text for the same FOV as depicted in (A): note the excellent correlation between suppressed superconductivity and position of columnar and clusters of point defects, marked by red and blue dashed circles, respectively.

Downloaded from https://www.science.org at Nanjing University on August 23, 2026

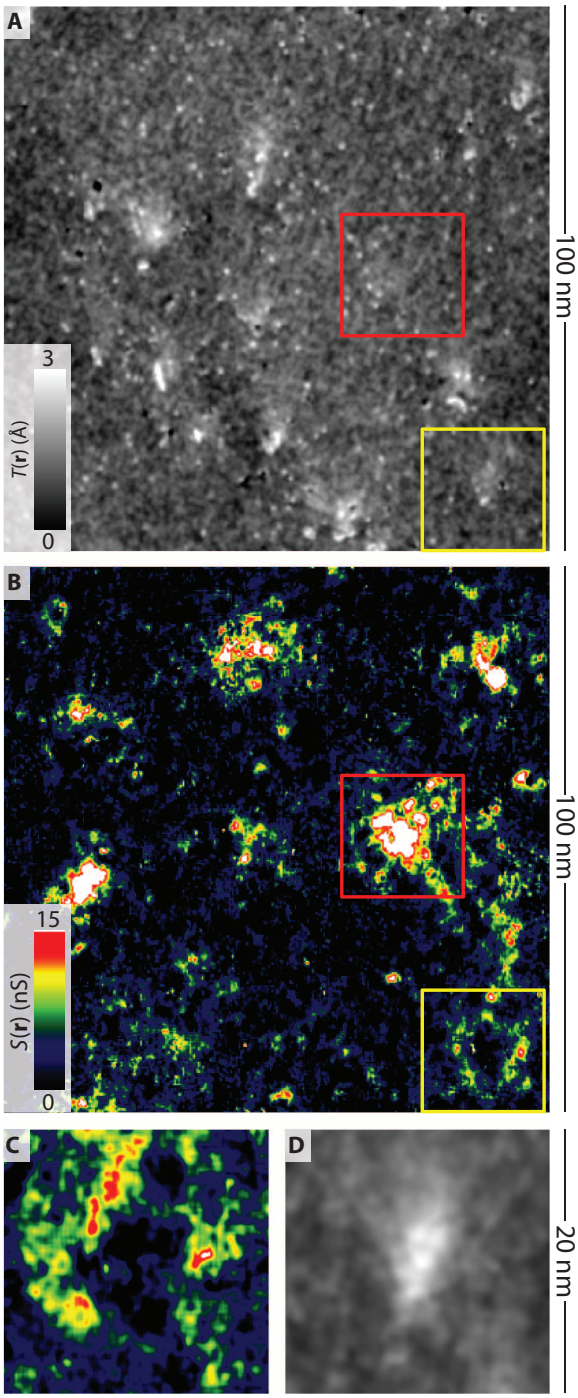

Fig. 3. Vortex halo surrounding columnar defects. (**A**) Constant current image $T(\mathbf{r})$: the red and yellow rectangles mark the position of vortices shown in (B). (**B**) $S(\mathbf{r})$ at 2 T of same FOV as in (A): the red rectangle marks a vortex that is far away from columnar defects, whereas the yellow rectangle encircles the halo of a vortex pinned to the columnar defect marked by the yellow rectangle in (A). (**C**) Average $S(\mathbf{r})$ of all columnar defects in (A): note the vortex halo surrounding a dark core because of the strong pinning of vortices to columnar defects at low fields. (**D**) Average $T(\mathbf{r})$ of all columnar defects in (A): the average columnar defect position agrees very well with the location of the pinning center deduced from the average vortex halo shown in (C).

these circumstances, the field dependence of the configuration of vortex core locations can be directly determined. Figure 4A shows a typical FOV for such B dependence studies, with Fig. 4B showing the ion-induced damage to the superconductivity as determined by measuring $F(\mathbf{r})$ simultaneously with Fig. 4A. The evolution of vortex locations with field is directly revealed in the measured $S(\mathbf{r},B)$ images as shown in Fig. 4 (C to H). Below the damage equivalent field of 2 T, the vortices are rarely detectable as a circular region in $S(\mathbf{r})$ as explained above

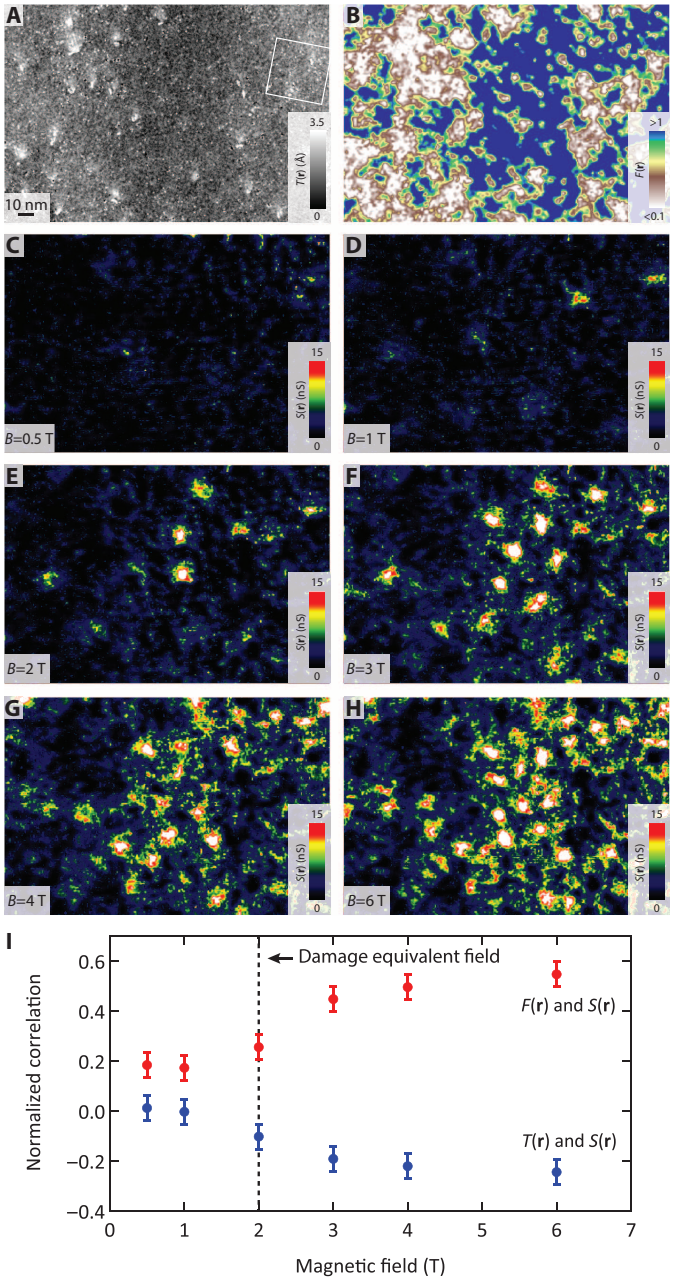

Fig. 4. Evolution of vortex configurations with magnetic field. (**A**) Constant current image $T(\mathbf{r})$ of same FOV studied in (B) to (H). (**B**) $F(\mathbf{r})$ of same FOV as in (A). (**C** to **H**) $S(\mathbf{r},B)$ for $B = 0.5, 1, 2, 3, 4$, and 6 T, respectively. (**I**) Normalized cross-correlation between $S(\mathbf{r})$ and $T(\mathbf{r})$ (blue), and $S(\mathbf{r})$ and $F(\mathbf{r})$ (red), as a function of field.

Downloaded from https://www.science.org at Nanjing University on August 23, 2026

(Fig. 3). Figure 4I shows the normalized cross-correlation of $F(\mathbf{r})$ with $S(\mathbf{r},B)$ in red, revealing that although there is little relation below 2 T, a strong positive correlation appears between regions of superconductivity [high $F(\mathbf{r})$] and the vortex signature $S(\mathbf{r},B)$ at higher fields. The related anti-correlation at high fields of the topograph $T(\mathbf{r})$ (Fig. 4A) and $S(\mathbf{r},B)$ is shown in blue and occurs because the regions of unperturbed superconductivity occur where little damage is detected in $T(\mathbf{r})$.

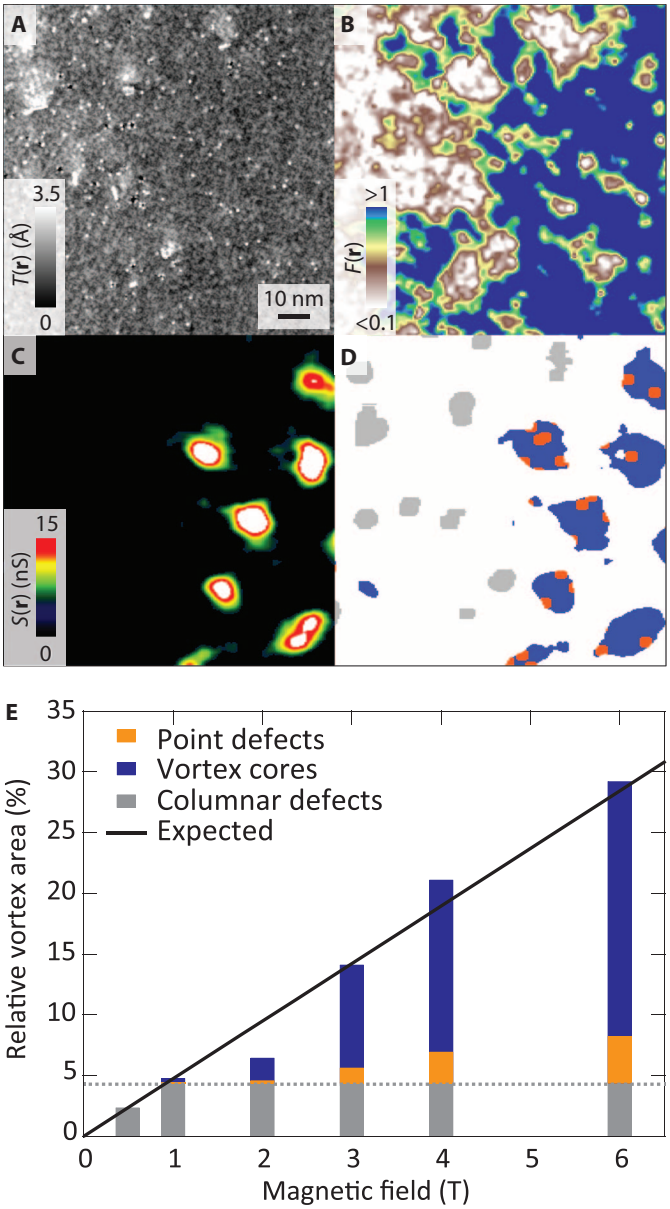

Fig. 5. Overview of vortex pinning sequence. (**A**) Constant current image $T(\mathbf{r})$ taken on irradiated Fe(Se,Te), clearly showing the columnar defects and point defects. (**B**) $F(\mathbf{r})$ in the same FOV as (A), illustrating the effect of the two types of defect on the superconducting tunneling signature. (**C**) Vortex image, $S(\mathbf{r})$, taken at 3 T on the area of (A). (**D**) Color-coded breakdown of the interplay of irradiation-induced defects, suppression of the spectral signature of superconductivity, and vortex pinning. Note the overlap between vortices (blue) far away from columnar defects (gray) and point defects (orange). The vortex density is the area in percentage of the full FOV covered by the various features. (**E**) Histogram representing the relation between vortices, columnar defects, and point defects distributed in a random, mixed pinning landscape created by swift ion irradiation. Data in the histogram were obtained by analysis of the whole FOV depicted in Fig. 4.

The interplay between ion-induced crystal damage, the heterogeneous superconductivity, and pinning of vortices revealed by these studies can be summarized as in Fig. 5. Figure 5A shows typical $T(\mathbf{r})$ with about eight columnar defects plus many point defects. Despite the negligible impact on the superconducting T_C, the local superconductivity as estimated using $F(\mathbf{r})$ can be greatly affected (Fig. 5B). Although this effect is pronounced at columnar defects, the point defects, when occurring at high density, also have strong effects on $F(\mathbf{r})$. Then, from the field dependence studies (Fig. 5C), we conclude that vortices are first very strongly pinned to the metallic core columnar defects where the spectral signature of superconductivity is eradicated. This number is fixed and represented in Fig. 5D by about eight gray patches and in Fig. 5E by gray components of the columns. At higher fields, observation of a strongly disordered vortex lattice appearing between the columnar defect sites indicates additional vortex pinning by clusters of point defects represented by orange circles in Fig. 5D and orange components of the columns in Fig. 5E. Finally, at highest fields, vortices begin to populate the areas of undamaged superconductivity and are therefore collectively pinned as shown as dark blue patches in Fig. 5D and similar color components of the columns in Fig. 5E. Thus, the evolution of vortex configurations in a single FOV (for example, Fig. 4) can be understood as a sequence of these three pinning processes.

Overall, our studies reveal that a picture of vortices localized at damage tracks of the size of the coherence length in an otherwise unaffected superconductor is oversimplified. Instead, superconductivity is affected on a much larger scale, and a mixed pinning landscape is obtained where the strongest pinning occurs at the columnar defect sites, which, on average, are the size of the coherence length as evidenced by the vortex halos we observe around them, and secondary pinning at clusters of point-like defects. Our finding that the amorphous cores of the Fe(Se,Te) columnar defects are metallic is significant because such cores exhibit quite different pinning potentials compared to those that are insulating, due to the distinct influence of the superconducting proximity effect (*8*, *9*). The discovery of such a complex mixed pinning landscape in high-energy ion irradiated Fe(Se,Te) is also important because such a situation suppresses detrimental "double-kink" vortex creep (*25*, *26*), enabling even higher values for J_C than in a scenario with columnar defects alone. Moreover, the novel combination of techniques that we introduce for simultaneous visualization of defects and superconductivity and vortex configurations can greatly aid in predictive engineering of vortex matter in high-temperature superconductors. This is because, in the future, such measured spatial shapes and high energy–resolution spectral fingerprints of both vortices and heavy ion–induced defects, in combination with realistic multiband Bogoliubov-deGennes theory (*27*) representing the identical real electronic environment, will be able to yield quantitative microscopic input parameters for massive Ginzburg-Landau–type simulations of optimal vortex pinning. Finally, by using this same approach, one could also pursue similar objectives in other materials such as cuprate high-T_C superconductors.

MATERIALS AND METHODS

High-quality $FeSe_{0.45}Te_{0.55}$ single crystals were grown at Brookhaven National Laboratory. The samples were irradiated at room temperature at the Laboratori Nazionali di Legnaro of the Istituto Nazionale di Fisica

Downloaded from https://www.science.org at Nanjing University on August 23, 2026

Nucleare, Italy, using 249-MeV Au^{17+} ions with a fluence $N = 1.93 \times 10^{15} m^{-2}$. The beam current was 0.2 nA with a 0.56-cm^2 spot (*28*). Magnetization measurements of both pristine and irradiated samples before insertion into the STM show a sharp transition with $T_C = 14 \pm 0.5$ K (see section I of the Supplementary Materials for more details). The samples were mechanically cleaved in cryogenic ultrahigh vacuum at T ~20 K and directly inserted into the STM head at 4.2 K. Stable and etched atomically sharp tungsten tips with energy-independent density of states were used. Differential conductance measurements throughout used a standard lock-in amplifier. All topographic data shown were taken at $E = -50$ mV and $I = 50$ pA.

SUPPLEMENTARY MATERIALS

Supplementary material for this article is available at http://advances.sciencemag.org/cgi/content/full/1/4/e1500033/DC1

Fig. S1. Magnetization and critical current density.
Fig. S2. Columnar and point defects in more detail.
Fig. S3. Crystal structure of the columnar defects.
Fig. S4. $F(\mathbf{r})$ for pristine and irradiated Fe(Se,Te) compared.
Fig. S5. Effect of point defects on superconductivity.
Fig. S6. High-energy (normal-state) characteristics of damage.
Fig. S7. Vortex halos at columnar defects.

REFERENCES AND NOTES

1. J. Paglione, R. L. Greene, High-temperature superconductivity in iron-based materials. *Nat. Phys.* **6**, 645–658 (2010).
2. L. Fang, Y. Jia, V. Mishra, C. Chaparro, V. K. Vlasko-Vlasov, A. E. Koshelev, U. Welp, G. W. Crabtree, S. Zhu, N. D. Zhigadlo, S. Katrych, J. Karpinski, W. K. Kwok, Huge critical current density and tailored superconducting anisotropy in $SmFeAsO_{0.8}F_{0.15}$ by low-density columnar-defect incorporation. *Nat. Commun.* **4**, 2655 (2013).
3. H. Q. Yuan, J. Singleton, F. F. Balakirev, S. A. Baily, G. F. Chen, J. L. Luo, N. L. Wang, Nearly isotropic superconductivity in $(Ba,K)Fe_2As_2$. *Nature* **457**, 565–568 (2009).
4. A. Gurevich, Iron-based superconductors at high magnetic fields. *Rep. Prog. Phys.* **74**, 124501 (2011).
5. Y. Kamihara, Current status of iron-based superconductors, in *ICAME 2011: Proceedings of the 31st International Conference on the Applications of the Mössbauer Effect (ICAME 2011) held in Tokyo, Japan, 25-30 September 2011*, Y. Yoshida, Ed. (Springer Netherlands, Dordrecht, Netherlands, 2013), pp. 703–711.
6. L. Civale, A. D. Marwick, T. K. Worthington, M. A. Kirk, J. R. Thompson, L. Krusin-Elbaum, Y. Sun, J. R. Clem, F. Holtzberg, Vortex confinement by columnar defects in $YBa_2Cu_3O_7$ crystals: Enhanced pinning at high fields and temperatures. *Phys. Rev. Lett.* **67**, 648–651 (1991).
7. F. Laviano, R. Gerbaldo, G. Ghigo, L. Gozzelino, G. P. Mikitik, T. Taen, T. Tamegai, Evidence of anisotropic vortex pinning by intrinsic and irradiation-induced defects in $Ba(Fe,Co)_2 As_2$ studied by quantitative magneto-optical imaging. *Supercond. Sci. Technol.* **27**, 044014 (2014).
8. S. M. Maurer, N.-C. Yeh, T. A. Tombrello, Vortex pinning by cylindrical defects in type-II superconductors: Numerical solutions to the Ginzburg-Landau equations. *Phys. Rev. B* **54**, 15372–15379 (1996).
9. B. Rosenstein, I. Shapiro, E. Deutch, B. Ya. Shapiro, Microwave absorption in the cores of Abrikosov vortices pinned by artificial insulator inclusion. *Phys. Rev. B* **84**, 134521 (2011).
10. Y. Zhu, Z. X. Car, R. C. Budhani, M. Suenaga, D. O. Welch, Structures and effects of radiation damage in cuprate superconductors irradiated with several-hundred-MeV heavy ions. *Phys. Rev. B* **48**, 6436 (1993).
11. Y. Yan, M. A. Kirk, Observation and mechanism of local oxygen reordering induced by high-energy heavy-ion (U^+, Au^+, Xe^+) irradiation in the high-T_c superconductor $YBa_2Cu_3O_{7-\delta}$. *Phys. Rev. B* **57**, 6152 (1998).
12. Y. Nakajima, Y. Tsuchiya, T. Taen, T. Tamegai, S. Okayasu, M. Sasase, Enhancement of critical current density in Co-doped $BaFe_2As_2$ with columnar defects introduced by heavy-ion irradiation. *Phys. Rev. B* **80**, 012510 (2009).
13. J. D. Moore, L. F. Cohen, Y. Yeshurun, A. D. Caplin, K. Morrison, K. A. Yates, C. M. McGilvery, J. M. Perkins, D. W. McComb, C. Trautmann, Z. A. Ren, J. Yang, W. Lu, X. L. Dong, Z. X. Zhao, The effect of columnar defects on the pinning properties of $NdFeAsO_{0.85}$ conglomerate particles. *Supercond. Sci. Technol.* **22**, 125023 (2009).
14. L. Fang, Y. Jia, C. Chaparro, G. Sheet, H. Claus, M. A. Kirk, A. E. Koshelev, U. Welp, G. W. Crabtree, W. K. Kwok, S. Zhu, H. F. Hu, J. M. Zuo, H.-H. Wen, B. Shen, High, magnetic field independent critical currents in $(Ba,K)Fe_2As_2$ crystals. *Appl. Phys. Lett.* **101**, 012601 (2012).
15. S. Behler, S. H. Pan, P. Jess, A. Baratoff, H.-J. Güntherodt, F. Lévy, G. Wirth, J. Wiesner, Vortex pinning in ion-irradiated $NbSe_2$ studied by scanning tunneling microscopy. *Phys. Rev. Lett.* **72**, 1751–1753 (1994).
16. A. M. Troyanovski, J. Aarts, P. H. Kes, Collective and plastic vortex motion in superconductors at high flux densities. *Nature* **399**, 665–668 (1999).
17. F.-C. Hsu, J.-Y. Luo, K.-W. Yeh, T.-K. Chen, T.-W. Huang, P. M. Wu, Y.-C. Lee, Y.-L. Huang, Y.-Y. Chu, D.-C. Yan, M.-K. Wu, Superconductivity in the PbO-type structure α-FeSe. *Proc. Natl. Acad. Sci. U. S.A.* **105**, 14262–14264 (2008).
18. H. Lei, R. Hu, E. S. Choi, J. B. Warren, C. Petrovic, Pauli-limited upper critical field of $Fe_{1+y}Te_{1-x}Se_x$. *Phys. Rev. B* **81**, 094518 (2010).
19. J.-F. Ge, Z.-L. Liu, C. Liu, C.-L. Gao, D. Qian, Q.-K. Xue, Y. Liu, J.-F. Jia, Superconductivity above 100 K in single-layer FeSe films on doped $SrTiO_3$. *Nat. Mater.* **14**, 285–289 (2015).
20. S. H. Pan, E. W. Hudson, J. C. Davis, ^{3}He refrigerator based very low temperature scanning tunneling microscope. *Rev. Sci. Instrum.* **70**, 1459–1463 (1999).
21. F. Massee, S. de Jong, Y. Huang, J. Kaas, E. van Heumen, J. B. Goedkoop, M. S. Golden, Cleavage surfaces of the $BaFe_{2-x}Co_xAs_2$ and $Fe_ySe_{1-x}Te_x$ superconductors: A combined STM plus LEED study. *Phys. Rev. B* **80**, 140507(R) (2009).
22. X. He, G. Li, J. Zhang, A. B. Karki, R. Jin, B. C. Sales, A. S. Sefat, M. A. McGuire, D. Mandrus, E. W. Plummer, Nanoscale chemical phase separation in $FeTe_{0.55}Se_{0.45}$ as seen via scanning tunneling spectroscopy. *Phys. Rev. B* **83**, 220502(R) (2011).
23. T. Hanaguri, S. Niitaka, K. Kuroki, H. Takagi, Unconventional *s*-wave superconductivity in Fe(Se,Te). *Science* **328**, 474–476 (2010).
24. T. Kato, Y. Mizuguchi, H. Nakamura, T. Machida, H. Sakata, Y. Takano, Local density of states and superconducting gap in the iron chalcogenide superconductor $Fe_{1+\delta}Se_{1-x}Te_x$ observed by scanning tunneling spectroscopy. *Phys. Rev. B* **80**, 180507(R) (2009).
25. D. R. Nelson, V. M. Vinokur, Boson localization and correlated pinning of superconducting vortex arrays. *Phys. Rev. B* **48**, 13060 (1993).
26. B. Maiorov, S. A. Baily, H. Zhou, O. Ugurlu, J. A. Kennison, P. C. Dowden, T. G. Holesinger, S. R. Foltyn, L. Civale, Synergetic combination of different types of defect to optimize pinning landscape using $BaZrO_3$-doped $YBa_2Cu_3O_7$. *Nat. Mater.* **8**, 398–404 (2009).
27. P. G. de Gennes, *Superconductivity of Metals and Alloys* (Benjamin, New York, 1966).
28. R. Gerbaldo, F. Laviano, G. Ghigo, L. Gozzelino, B. Minetti, A. Rovelli, E. Mezzetti, Nanostructuring YBCO thin films by heavy-ion beam for local magnetic field and infrared photon detection. *Nucl. Instr. Meth. B* **272**, 291–295 (2012).

Funding: Experimental studies are supported by the Center for Emergent Superconductivity, an Energy Frontier Research Center, headquartered at Brookhaven National Laboratory and funded by the U.S. Department of Energy, under DE-2009-BNL-PM015. Irradiations were performed in the framework of the INFN-Politecnico di Torino M.E.S.H. experiment. **Author contributions:** F.M. and P.O.S. performed STM measurements and data analysis. Y.-L.W. performed the magnetization and J_c measurements and G. Ghigo performed irradiation with Au ions. G. D. Gu synthesized Fe(Se,Te) samples. J.C.D. and W.-K.K. designed and supervised project. **Competing interests:** The authors declare that they have no competing interests.

Submitted 9 January 2015
Accepted 13 April 2015
Published 22 May 2015
10.1126/sciadv.1500033

Citation: F. Massee, P. O. Sprau, Y. -L. Wang, J. C. Davis, G. Ghigo, G. D. Gu, W.-K. Kwok, Imaging atomic-scale effects of high-energy ion irradiation on superconductivity and vortex pinning in Fe(Se,Te). *Sci. Adv.* **1**, e1500033 (2015).

Downloaded from https://www.science.org at Nanjing University on August 23, 2026

Science Advances

Imaging atomic-scale effects of high-energy ion irradiation on superconductivity and vortex pinning in Fe(Se,Te)

Freek Massee, Peter Oliver Sprau, Yong-Lei Wang, J. C. Séamus Davis, Gianluca Ghigo, Genda D. Gu, and Wai-Kwong Kwok

Sci. Adv. **1** (4), e1500033. DOI: 10.1126/sciadv.1500033

View the article online
https://www.science.org/doi/10.1126/sciadv.1500033
Permissions
https://www.science.org/help/reprints-and-permissions

Downloaded from https://www.science.org at Nanjing University on August 23, 2026

Use of this article is subject to the Terms of service

Science Advances (ISSN 2375-2548) is published by the American Association for the Advancement of Science. 1200 New York Avenue NW, Washington, DC 20005. The title *Science Advances* is a registered trademark of AAAS.

Copyright © 2015, The Authors